

Article

Bidirectional Operation Scheme of Grid-Tied Zeta Inverter for Energy Storage Systems

Woo-Young Choi

Division of Electronic Engineering, Jeonbuk National University, Jeonju 561-756, Korea; wychoi@jbnu.ac.kr;
Tel.: +82-063-270-4218

Received: 7 June 2020; Accepted: 16 July 2020; Published: 17 July 2020



Abstract: The zeta inverter has been used for single-phase grid-tied applications. For its use of energy storage systems, this paper proposes the bidirectional operation scheme of the grid-tied zeta inverter. A shoot-through switching state is introduced, providing reliable bidirectional operation modes. A shoot-through duty cycle is utilized for the bidirectional grid current control of the inverter. The grid current is bidirectionally controlled by the shoot-through duty cycle, which enables the inverter to operate with seamless change of operation modes. Over the state-of-the-art techniques using flyback and Cuk inverter topologies, the grid-tied zeta inverter using the proposed operation scheme provides advantages of high efficiency, low cost, and high reliability. The operation principle is presented by describing the operation mode and control method for the grid-tied zeta inverter. A 500 W prototype has been built and tested to verify its operation principle.

Keywords: grid-tied zeta inverter; energy storage systems; bidirectional operation; shoot-through; switching state; duty cycle

1. Introduction

Up to now, various single-phase isolated grid-tied inverters have been developed with renewable energy sources [1–10]. Among them, the grid-tied zeta inverter has been recently developed for high-efficiency inverter designs [7–10]. It has been gaining high attention due to its circuit count reduction design [9,10]. As the state-of-the-art techniques, the grid-tied flyback inverter [1–3] and the grid-tied Cuk inverter [4–6] necessarily use a bidirectional switch along with the unfolding switching circuit at the grid side. It needs the additional gate driving circuit, which causes drawbacks for increasing the manufacturing cost and decreasing the power density for industrial uses. On the other hand, the grid-tied zeta inverter can solve the drawbacks of the current state-of-the-art inverters because it does not use the bidirectional switch at the grid side [9,10]. It can reduce the circuit components and improve the power density. Furthermore, it can increase the power efficiency for reducing the switching loss by removing the bidirectional switch, compared to the previous bidirectional grid-tied inverters using flyback and Cuk inverter topologies. As the grid-tied zeta inverter operates in the continuous conduction mode [9], it has reduced conduction losses, compared to the inverters operating in the discontinuous conduction mode [7,8]. Furthermore, the grid-tied zeta inverter has improved its power efficiency [10] by using advanced switching techniques such as active clamp [11] and synchronous rectification [12].

One thing to remark is that its most applications have been mainly focused on photovoltaic power generations [7–10]. As a microinverter for photovoltaic modules, the grid-tied zeta inverter operates as an isolated dc-ac converter, supplying ac power from dc power source. However, for its use of energy storage systems, the grid-tied zeta inverter needs a bidirectional operation scheme. In the energy storage systems, the grid-tied zeta inverter should interface the grid with energy storage devices such

as batteries [13] and ultracapacitors [14]. Nevertheless, any literatures have not been reported yet about the bidirectional operation of the grid-tied zeta inverter.

This paper proposes the bidirectional operation scheme of the grid-tied zeta inverter for energy storage systems. The operation principle is presented for its operation mode and control method. A shoot-through switching state [15] is intentionally introduced for the bidirectional operation of the inverter. The shoot-through is typically a forbidden switching state for isolated grid-tied inverters because of the breakdown of the full-bridge unfolding circuit [16,17]. In contrast, the shoot-through switching state provides reliable bidirectional operation modes for the grid-tied zeta inverter. A shoot-through duty cycle is utilized for the bidirectional grid current control of the inverter. The grid current can be bidirectionally controlled by the shoot-through duty cycle. A unified grid current controller can be implemented, which enables the grid-tied zeta inverter to have seamless change of operation modes [18,19].

In this paper, Section 2 presents the operation principle of the grid-tied zeta inverter. It describes the circuit configuration, operation mode, and control method. Section 3 discusses the experiment results to verify the operation principle for a 500 W prototype. Section 4 presents the concluding remark of the paper.

2. Proposed Inverter

2.1. Circuit Configuration

Figure 1 shows the circuit diagram of the grid-tied zeta inverter for energy storage systems. The grid-tied zeta inverter has a primary switch (S_P), a high-frequency transformer (T), and a secondary switching circuit ($C_S, S_{S1}, S_{S2}, S_{S3}, S_{S4}, L_g$). The dc voltage for the energy storage device is V_b . The grid voltage v_g is defined as

$$v_g = V_g \sin \omega t. \quad (1)$$

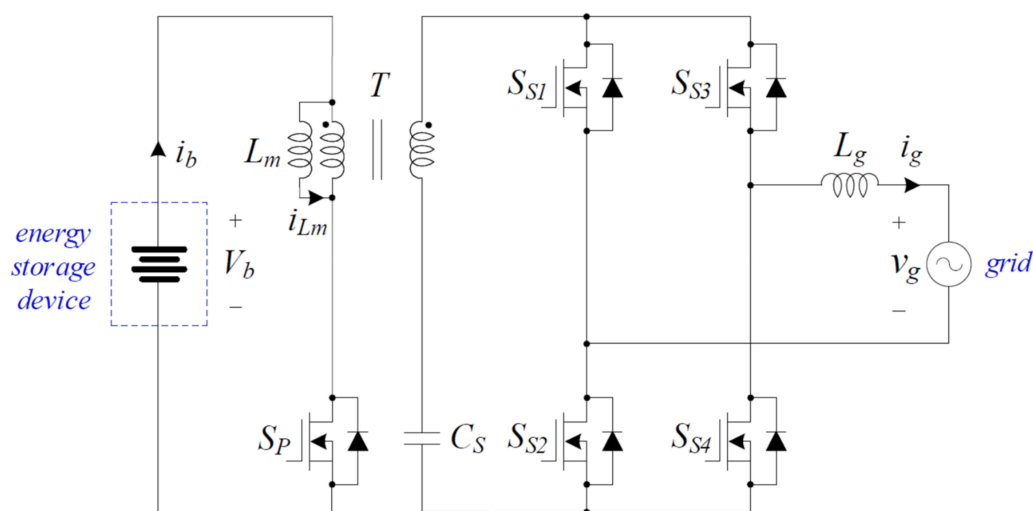


Figure 1. Circuit diagram of the grid-tied zeta inverter for energy storage systems.

The absolute peak value of v_g is V_g . The angular frequency of v_g is ω . An ideal transformer is modeled as T , which has the magnetizing inductor L_m with a negligible leakage inductor. Its turns ratio n is n_s/n_p . The primary winding turns is n_p . The secondary winding turns is n_s . The magnetizing inductor L_m is large enough so that its current i_{Lm} is continuous during constant switching period T_s . The filter inductor L_g is large enough so that the grid current i_g is continuous during T_s . The secondary capacitor C_S is large enough so that its voltage V_{C_S} is constant during T_s . The capacitor voltage V_{C_S} is considered to be $|v_g|$ as the secondary switching circuit gives the current path to fold v_g .

All power switches are considered ideal with their intrinsic body diodes. A shoot-through switching state happens when series connected power switches are turned on simultaneously in the secondary switching circuit. One shoot-through switching state occurs when S_{S1} and S_{S2} are turned on simultaneously. Another shoot-through switching state occurs when S_{S3} and S_{S4} are turned on simultaneously. The LC network (L_m, C_S) couples the secondary switching circuit to the grid, thus providing reliable power transfer operation that cannot be obtained in the traditional isolated grid-tied inverters.

The grid-tied zeta inverter has two operation modes: the inverter mode and the rectifier mode. In the inverter mode, it operates as an isolated dc-ac converter, supplying the energy storage device power into the grid. In the rectifier mode, it operates as an isolated ac-dc converter, supplying the grid power into the energy storage device.

2.2. Operation Mode

Figure 2 shows the circuit diagrams that describe the switching states in the inverter mode. Figure 2a,b show the switching circuit diagrams during T_s , respectively, for the positive grid voltage. The switches S_{S2} and S_{S3} are always turned on, and S_{S4} is always turned off. The switch S_{S1} operates complementary to S_P with constant switching frequency $f_s (=1/T_s)$. There are four switching states in the inverter mode. It is a switching state 1 when S_{S1} is turned off and S_P is turned on, as shown in Figure 2a. The magnetizing inductor L_m stores the energy from V_b . As the voltage across the secondary winding of T is nV_b , the grid current i_g increases linearly at the rate of $di_g/dt = nV_b/L_g$. As shown in Figure 2b, it is a switching state 2 when S_{S1} is turned on and S_P is turned off. This is the shoot-through switching state that the energy stored in L_m is transferred to C_S through C_S, S_{S2}, S_{S1} , and the secondary winding of T . The grid current i_g freewheels through L_g, v_g, S_{S1} , and S_{S3} , decreasing at the rate of $di_g/dt = -v_g/L_g$.

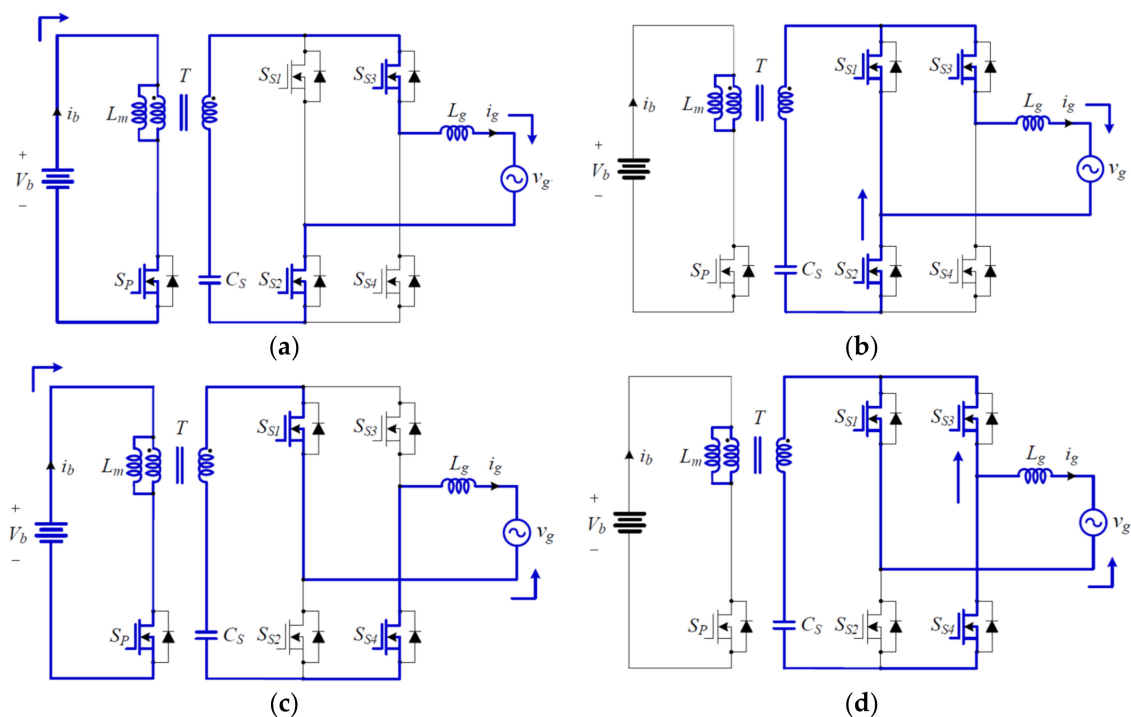


Figure 2. Switching states in the inverter mode: (a) state 1 for the positive grid voltage; (b) state 2 for the positive grid voltage; (c) state 3 for the negative grid voltage; (d) state 4 for the negative grid voltage.

Figure 2c,d show the switching circuit diagrams during T_s , respectively, for the negative grid voltage. The switches S_{S1} and S_{S4} are always turned on, and S_{S2} is always turned off. The switch S_{S3} operates complementary to S_P with f_s . It is a switching state 3 when S_{S3} is turned off and S_P is

turned on, as shown in Figure 2c. The magnetizing inductor L_m stores the energy from V_b . As the voltage across the secondary winding of T is nV_b , the grid current i_g decreases linearly at the rate of $di_g/dt = -nV_b/L_g$. As shown in Figure 2b, it is a switching state 4 when S_{S3} is turned on and S_P is turned off. This is the shoot-through switching state that the energy stored in L_m is transferred to C_S through C_S , S_{S4} , S_{S3} , and the secondary winding of T . The grid current i_g freewheels through L_g , v_g , S_{S1} , and S_{S3} , increasing at the rate of $di_g/dt = v_g/L_g$.

Figure 3 shows the circuit diagrams to describe the switching states in the rectifier mode. Figure 3a,b show the switching circuit diagrams during T_s , respectively, for the positive grid voltage. The switches S_{S2} and S_{S3} are always turned on, and S_{S4} is always turned off. The switch S_{S1} operates complementary to S_P with f_s . There are four switching states in the rectifier mode. It is a switching state 1 when S_{S1} is turned on and S_P is turned off, as shown in Figure 3a. This is the shoot-through switching state that the energy stored in C_S is transferred to L_m through S_{S1} , S_{S2} , C_S , and the secondary winding of T . The inductor L_g stores the energy from v_g . The grid current i_g increases linearly at the rate of $di_g/dt = v_g/L_g$. As shown in Figure 3b, it is a switching state 2 when S_{S1} is turned off and S_P is turned on. When S_P is turned on, L_m supplies its stored energy to V_b . As the voltage across L_m is V_b , i_g decreases linearly at the rate of $di_g/dt = -nV_b/L_g$.

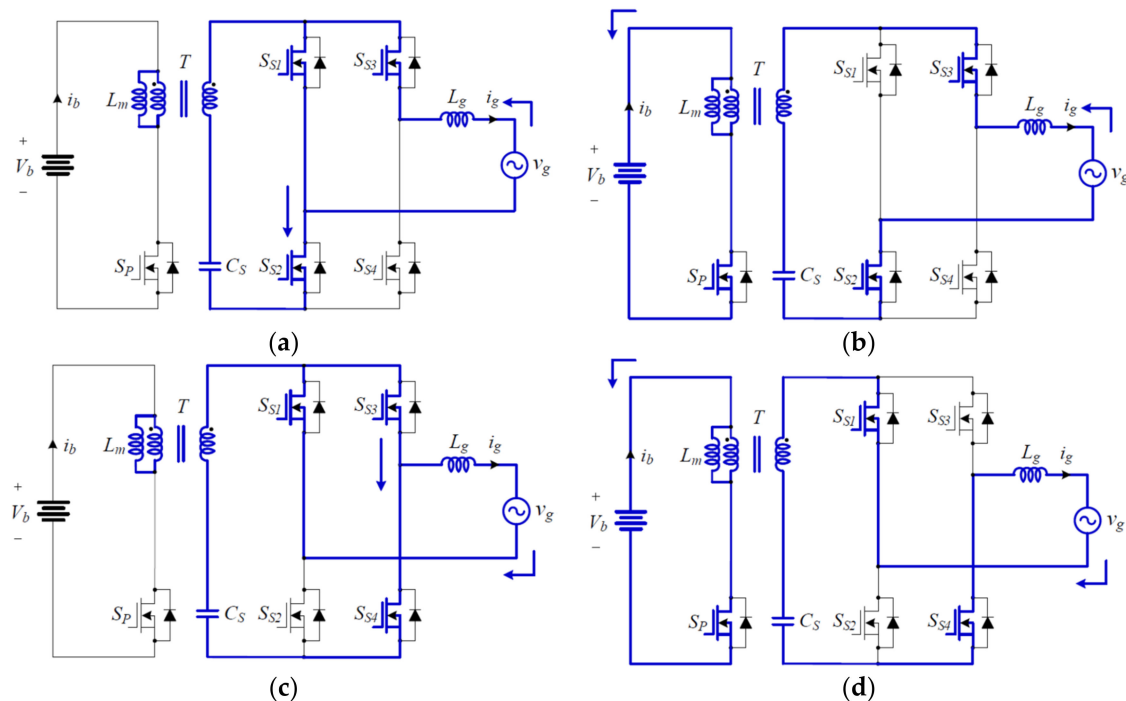


Figure 3. Switching states in the rectifier mode: (a) state 1 for the positive grid voltage; (b) state 2 for the positive grid voltage; (c) state 3 for the negative grid voltage; (d) state 4 for the negative grid voltage.

Figure 3c,d show the switching circuit diagrams during T_s , respectively, for the negative grid voltage. The switches S_{S1} and S_{S4} are always turned on, and S_{S2} is always turned off. The switch S_{S3} operates complementary to S_P with f_s . It is a switching state 3 when S_{S3} is turned on and S_P is turned off, as shown in Figure 3c. This is the shoot-through switching state that the energy stored in C_S is transferred to L_m through S_{S3} , S_{S4} , C_S , and the secondary winding of T . The inductor L_g stores the energy from v_g . The grid current i_g decreases linearly at the rate of $di_g/dt = -v_g/L_g$. As shown in Figure 3d, it is a switching state 4 when S_{S3} is turned off and S_P is turned on. When S_P is turned on, L_m supplies its stored energy to V_b . As the voltage across L_m is V_b , i_g increases linearly at the rate of $di_g/dt = nV_b/L_g$.

Assume that the shoot-through duty cycle is D_{ST} for T_s . Regardless of the operation modes, the on-time of S_{S1} is the shoot-through duty cycle for the positive grid voltage. For the negative grid

voltage, the on-time of S_{S3} is the shoot-through duty cycle. Suppose that the on-time of S_p is D_{SP} for T_s . As D_{SP} is complementary to D_{ST} for T_s , the following duty cycle relationship is obtained as

$$D_{SP} + D_{ST} = 1. \tag{2}$$

2.3. Control Method

Regardless of the operation modes, the volt-second balance for L_g during T_s gives the following voltage Equation as

$$v_g D_{ST} T_s - nV_b(1 - D_{ST}) T_s = 0. \tag{3}$$

By rearranging (3), we have the relation between v_g and V_b as

$$\frac{V_b}{v_g} = \frac{D_{ST}}{n(1 - D_{ST})}. \tag{4}$$

By (4) and the input-output power relation of $V_b i_b = v_g i_g$, we have the relation between i_b and i_g as

$$\frac{i_g}{i_b} = \frac{D_{ST}}{n(1 - D_{ST})}. \tag{5}$$

By the relation between i_b and i_{Lm} , the following current equation is represented as

$$i_b = (1 - D_{ST})i_{Lm}. \tag{6}$$

By (5) and (6), the relation between i_g and i_{Lm} is represented as

$$ni_b = D_{ST}i_{Lm}. \tag{7}$$

For both operation modes, the following voltage equations can be obtained for L_m for one switching period T_s as

$$-|v_g| = L_m \frac{i_{Lm}}{D_{ST}T_s}. \tag{8}$$

$$nV_b = L_m \frac{i_{Lm}}{(1 - D_{ST})T_s}. \tag{9}$$

By (8) and (9), the average voltage for L_m during T_s can be represented with respect to the deviation Δi_{Lm} of i_{Lm} as

$$-|v_g|D_{ST} + nV_b(1 - D_{ST}) = L_m \frac{\Delta i_{Lm}}{T_s}. \tag{10}$$

From (10), D_{ST} can be represented as

$$D_{ST} = \frac{nV_b}{nV_b + |v_g|} - \frac{1}{nV_b + |v_g|} \left(\frac{L_m \Delta i_{Lm}}{T_s} \right). \tag{11}$$

By using (4) and (7), D_{ST} in (11) can be represented as

$$D_{ST} = D_{N,ST} + D_{C,ST} = \frac{nV_b}{nV_b + |v_g|} - \frac{L_m \Delta i_g}{V_b T_s} \tag{12}$$

where $D_{N,ST}$ is the nominal shoot-through duty cycle, and $D_{C,ST}$ is the controlled shoot-through duty cycle as

$$D_{N,ST} = \frac{nV_b}{nV_b + |v_g|} = \frac{nV_b}{nV_b + V_g |\sin \omega t|}, D_{C,ST} = -\frac{L_m \Delta i_g}{V_b T_s}. \tag{13}$$

Suppose that v_g is exactly measured with a phase-locked loop (PLL) [20]. The nominal shoot-through duty cycle $D_{N,ST}$ plays the role of providing the nominal voltage compensation. For both operation modes, the relation between D_{ST} and i_g is nonlinear, as shown in (12). By using $D_{N,ST}$ for the nominal voltage compensator, the non-linear system in (12) is transformed to the first order linear system, which can be controlled by $D_{C,ST}$.

As the same nominal and controlled shoot-through duty cycles can be defined for both operation modes, the bidirectional grid current control can be performed in a unified controller. This feature enables the grid-tied zeta inverter to have seamless change of operation modes. Figure 4 shows the bidirectional grid current control block diagram of the grid-tied zeta inverter. The operation mode is selected by the sign of I_g^* . The power level is decided by the peak magnitude of the grid current reference I_g^* . A grid current controller generates $D_{C,ST}$ to minimize the error between i_g^* and i_g . The grid current controller can be designed by high performance grid current control techniques such as the proportional-resonant (PR) control [21] and the repetitive control [22].

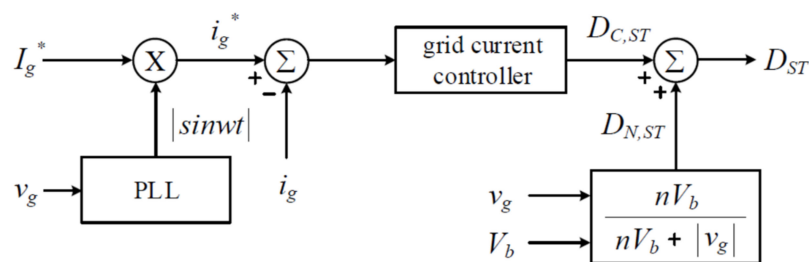


Figure 4. Bidirectional grid current control block diagram of the grid-tied zeta inverter.

2.4. Control Implementation

To regulate the grid current i_g with low harmonic currents, $D_{C,ST}$ can be implemented by the PR control [21]. Its ideal transfer function $C_{PR}(s)$ is

$$C_{PR}(s) = k_p + \frac{k_r s}{s^2 + \omega^2} \tag{14}$$

where k_p and k_r are PR control gains, respectively. Unfortunately, it is not able to implement the PR controller in (14) with an infinite gain. Therefore, the following non-ideal transfer function is used as

$$C_{PR}(s) = k_p + \frac{2k_r \omega_c s}{s^2 + 2\omega_c s + \omega^2} \tag{15}$$

where ω_c is the angular frequency at the cutoff frequency of the controller. Also, additional harmonic compensators could be included to the PR controller for minimizing the harmonic currents for selective harmonic frequencies [23]. Its transfer function $C_{HC}(s)$ can be represented as

$$C_{HC}(s) = \sum_{h=3, 5, 7} \frac{2k_{rh} \omega_c s}{s^2 + 2\omega_c s + (h\omega)^2} \tag{16}$$

where h is the harmonic order and k_{rh} is the resonant control gain for each harmonic frequency. Since the third, fifth, and seventh harmonics are significant under the grid environment, the third to seventh harmonic compensators would be implemented.

3. Experiment Results

A 500 W prototype has been built for the grid-tied zeta inverter. Table 1 shows the key parameters and components of the prototype. The prototype includes the power and control circuits as well as the auxiliary circuits for gate driving circuits and stand-by power circuit. For the energy storage device, value-regulated lead acid batteries have been used. Four 12-V batteries are connected in

series whose nominal voltage is 48 V. The PR control has been adopted for the grid current controller. Its digital implementation has been performed by a micro-controller dsPIC30F3011 (microchip). For the implementation of the transformer, a ferrite magnetic core (PQ5050) has been used with a bifilar winding technique so that the leakage inductance could be minimized.

Table 1. Key parameters and components.

Symbol	Quantity	Value
V_b	battery voltage	48 V
v_g	grid voltage	60 Hz/220 V _{rms}
f_s	switching frequency	50 kHz
L_m	magnetizing inductor	60 μ H
n_p	primary winding turns	15
n_s	secondary winding turns	64
C_s	secondary capacitor	1.0 μ F
L_g	filter inductor	2.0 mH
S_p	primary switch	IXFK150N30P3
$S_{S1} \sim S_{S4}$	secondary switches	UJC1206K

Figure 5 shows the experiment waveforms for the grid voltage v_g , the grid current i_g , and the battery voltage V_b . Figure 5a shows the experiment waveforms for 500 W in the inverter mode. The grid current i_g is in phase with v_g . The grid-tied zeta inverter operates as an isolated dc-ac converter, supplying the battery power into the grid. The total harmonic distortion was measured as 3.1%. Figure 5b shows the experiment waveforms for 500 W in the rectifier mode. The grid current i_g is 180° out of phase with v_g . The grid-tied zeta inverter operates as an isolated ac-dc converter, supplying the grid power into the battery. The total harmonic distortion was measured as 3.3%. For both operation modes, the power factor was measured as 0.99. As shown in Figure 5, the grid-tied zeta inverter performs its bidirectional operation with high power quality.

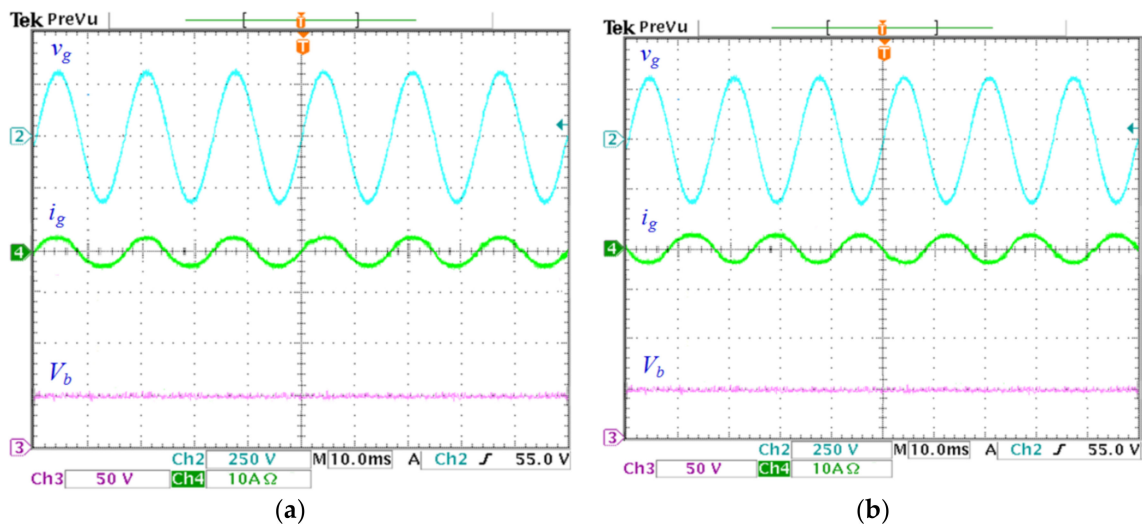


Figure 5. Experiment waveforms for the grid voltage v_g , the grid current i_g , and the battery voltage V_b : (a) waveforms in the inverter mode; (b) waveforms in the rectifier mode.

Figure 6 shows the experiment waveforms for the operation mode changes. Figure 6a shows the experiment waveforms for v_g and i_g for 500 W from the inverter mode to the rectifier mode. Figure 6b shows the experiment waveforms for v_g and i_g for 500 W from the rectifier mode to the inverter mode. As shown in Figure 6, the grid current i_g has been seamlessly changed as the inverter changes its operation mode. The grid-tied zeta inverter operates with seamless change of operation modes by the suggested control method.

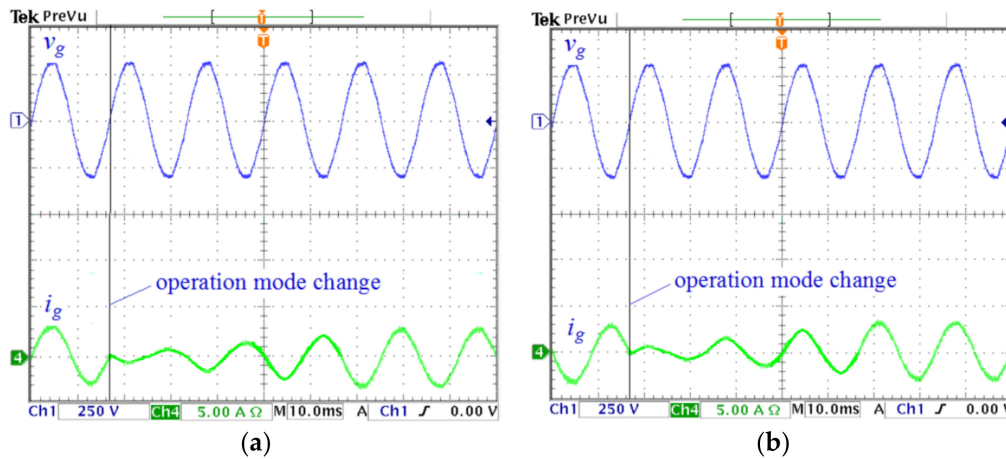


Figure 6. Experiment waveforms for the operation mode changes: (a) waveforms from the inverter mode to the rectifier mode; (b) waveforms from the rectifier mode to the inverter mode.

Figure 7 shows the measured power efficiency curves. The digital power meter (WT-230, Yokogawa Electric, Tokyo, Japan) has been used for the calculation and the measurement of the power efficiency. The power efficiency has been calculated by dividing the output power by the input power. The uncertainty level for the measured power efficiency ranges from -0.05% to 0.05% . The uncertainty has been determined by residual measurement error.

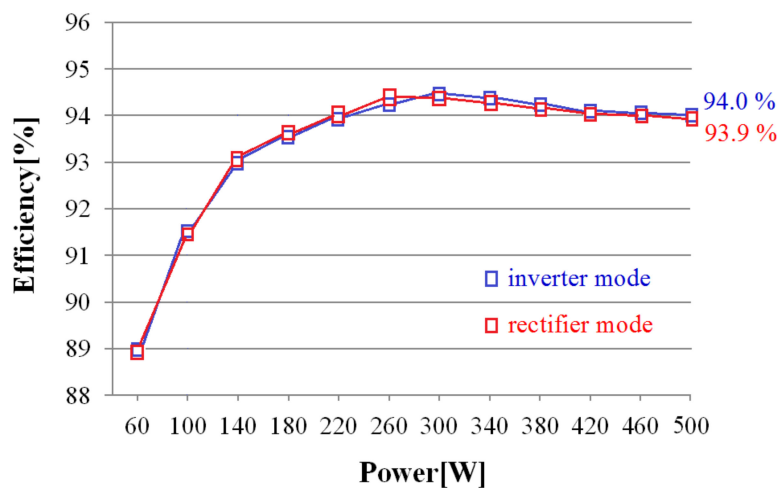


Figure 7. Measured power efficiency curves.

The blue curve shows the power efficiency curve in the inverter mode. The grid-tied zeta inverter has shown the peak efficiency of 94.5% at 300 W . It has achieved the efficiency of 94.0% at 500 W . The red curve shows the power efficiency curve in the rectifier mode. The grid-tied zeta inverter has shown the peak efficiency of 94.3% at 260 W . It has achieved the efficiency of 93.9% at 500 W . As the inverter operates for entire load conditions, ranging from light load to full load, the prototype has been designed to achieve its peak efficiency around half of the rated load condition. The peak efficiency point can be mainly changed by the key circuit components such as the power switches and the reactive components.

4. Concluding Remark

This paper has proposed the bidirectional operation scheme of the grid-tied zeta inverter for energy storage systems. The operation principle has been presented for the operation mode and control method. A shoot-through switching state has been introduced, providing reliable bidirectional

operation modes for the inverter. A shoot-through duty cycle has been utilized for the bidirectional grid current control. A unified grid current controller has been implemented, which enables the grid-tied zeta inverter to perform seamless change of operation modes. A 500 W prototype has been built and tested to verify its operation principle. The grid-tied zeta inverter has achieved the peak efficiency of 94.5% at 300 W and the efficiency of 94.0% at 500 W, respectively, in the inverter mode. It has achieved the peak efficiency of 94.3% at 300 W and the efficiency of 93.9% at 500 W, respectively, in the rectifier mode. The grid-tied zeta inverter with the proposed operation scheme can provide benefits such as high efficiency, low cost, and high reliability over the previous inverter techniques. It is expected that the proposed operation principle enables the grid-tied zeta inverter to be a next-generation inverter technique, which can reduce the manufacturing cost and provide high power efficiency for energy storage systems.

As a future research, several topics would be considered for renewable energy and smart grid integrations. In terms of control-level research, the output impedance of the inverter could be controlled. For power flow control, more research efforts should be made for parallel operation of inverters. In terms of circuit-level research, the use of gallium-nitride (GaN) power devices should be considered for the design of inverters. Along with the use of the advanced power devices, the use of high frequency switching device like planar transformers would facilitate developing high power density design of the inverters.

Author Contributions: W.-Y.C. managed the project, performed the experiments, analyzed the data, and wrote the manuscript. The Author has read and agreed to the published version of the manuscript.

Funding: This work was supported by the National Research Foundation of Korea (NRF) grant funded by the Korea government (MSIT) (2020R1F1A1048346). Also, this research was supported by “Research Base Construction Fund Support Program” funded by Jeonbuk National University in 2020.

Conflicts of Interest: The author declares no potential conflict of interest.

References

1. Dong, M.; Tian, X.; Li, L.; Song, D.; Wang, L.; Zhao, M. Model-based current sharing approach for DCM interleaved flyback microinverter. *Electronics* **2018**, *11*, 1685.
2. Feng, X.; Wang, F.; Wu, C.; Luo, J.; Zhang, L. Modeling and comparisons of aggregated flyback microinverters in aspect of harmonic resonances with the grid. *IEEE Trans. Ind. Electron.* **2019**, *66*, 276–285. [[CrossRef](#)]
3. Lodh, T.; Pragallapati, N.; Agarwal, V. Novel control scheme for an interleaved flyback converter based solar PV microinverter to achieve high efficiency. *IEEE Trans. Ind. Appl.* **2018**, *54*, 3473–3482. [[CrossRef](#)]
4. Han, B.; Lee, J.S.; Kim, M.S. Repetitive controller with phase-lead compensation for Cuk CCM inverter. *IEEE Trans. Ind. Electron.* **2018**, *65*, 2356–2367. [[CrossRef](#)]
5. Han, B.; Lai, J.-S.; Kim, M.S. Bridgeless Cuk-derived single power conversion inverter with reactive-power capability. *IEEE Trans. Power Electron.* **2020**, *35*, 2629–2645. [[CrossRef](#)]
6. Han, B.; Lai, J.-S.; Kim, M.S. Dynamic modeling and controller design of dual-mode Cuk inverter in grid-connected PV/TE applications. *IEEE Trans. Power Electron.* **2018**, *33*, 8887–8904. [[CrossRef](#)]
7. Viero, R.C.; Lopez, H.F.M.; Zollmann, C.A.; dos Reis, F.S. Dynamic modeling of a sinusoidal inverter based on zeta converter working in DCM for PV arrays. In Proceedings of the Annual Conference on IEEE Industrial Electronics Society (IECON), Glendale, AZ, USA, 7–10 November 2010; pp. 439–444.
8. Levin, G.H.; Flores, J.V.; Salton, A.; dos Reis, F.S. Internal model control of the zeta converter for the grid connection of photovoltaic panels. In Proceedings of the Brazilian Power Electronics Conference, Gramado, Brazil, 27–31 October 2013; pp. 666–671.
9. Surapaneni, R.K.; Rathore, A.K. A single-stage CCM zeta microinverter for solar photovoltaic AC module. *IEEE J. Emerg. Sel. Topics Power Electron.* **2015**, *3*, 892–900. [[CrossRef](#)]
10. Choi, W.Y.; Yang, M.K. High-efficiency design and control of zeta inverter for single-phase grid-connected applications. *Energies* **2019**, *12*, 974. [[CrossRef](#)]
11. Liu, Y.C.; Chen, M.C.; Yang, C.Y.; Kim, K.A.; Chiu, H.J. High-efficiency isolated photovoltaic microinverter using wide-band gap switches for standalone and grid-tied applications. *Energies* **2018**, *11*, 569. [[CrossRef](#)]

12. Liu, Y.C.; Chen, M.C.; Yang, C.Y.; Kim, K.A.; Chiu, H.J. Research on digital synchronous rectification for a high-efficiency dc-dc converter in an auxiliary power supply system of magnetic levitation. *Energies* **2020**, *13*, 51.
13. Sandelic, M.; Sangwongwanich, A.; Blaabjerg, F. Reliability evaluation of PV systems with integrated battery energy storage systems: Dc-coupled and ac-coupled configurations. *Electronics* **2019**, *8*, 1059. [[CrossRef](#)]
14. Fang, J.; Tang, Y.; Li, H.; Li, X. A battery/ultracapacitor hybrid energy storage system for implementing the power management of virtual synchronous generators. *IEEE Trans. Power Electron.* **2018**, *33*, 2820–2824. [[CrossRef](#)]
15. Lai, R.; Wang, F.; Burgos, R.; Boroyevich, D.; Zhang, D.; Ning, P. A shoot-through protection scheme for converters built with SiC JFETs. *IEEE Trans. Ind. Appl.* **2010**, *46*, 2495–2500. [[CrossRef](#)]
16. Caiza, D.L.; Kouro, S.; Flores-Bahamonde, F.; Hernandez, R. Unfolding PV microinverter current control: Rectified sinusoidal vs sinusoidal reference waveform. In Proceedings of the Annual Conference on IEEE Energy Conversion Congress and Exposition (ECCE), Portland, OR, USA, 7–10 September 2018; pp. 7094–7100.
17. Hernandez-Vidal, R.; Renaudineau, H.; Kouro, S. Sub-module photovoltaic microinverter with cascaded flybacks and unfolding H-bridge inverter. In Proceedings of the Annual Conference on IEEE International Symposium on Industrial Electronics (ISIE), Edinburgh, UK, 19–21 June 2017; pp. 1035–1040.
18. Kim, N.; Parkhideh, B. PV-battery series inverter architecture: A solar inverter for seamless battery integration with partial-power dc-dc optimizer. *IEEE Trans. Energy Convers.* **2019**, *34*, 478–485. [[CrossRef](#)]
19. Dong, D.; Thacker, T.; Cvetkovic, I.; Burgos, R.; Boroyevich, D.; Wang, F.; Skutt, G. Modes of operation and system-level control of single-phase bidirectional PWM converter for microgrid systems. *IEEE Trans. Smart Grid* **2012**, *3*, 93–104. [[CrossRef](#)]
20. Tan, G.; Zong, C.; Sun, X. Tan-Sun transformation-based phase-locked loop in detection of the grid synchronous signals under distorted grid conditions. *Electronics* **2020**, *9*, 674. [[CrossRef](#)]
21. Zmood, D.N.; Holmes, D.G. Stationary frame current regulation of PWM inverters with zero steady-state error. *IEEE Trans. Power Electron.* **2003**, *18*, 814–822. [[CrossRef](#)]
22. Jiang, S.; Cao, D.; Li, Y.; Liu, J.; Peng, F.Z. Low-THD, fast-transient, and cost-effective synchronous-frame repetitive controller for three-phase UPS inverters. *IEEE Trans. Power Electron.* **2012**, *27*, 2139–2149. [[CrossRef](#)]
23. Pereira, L.F.A.; Flores, J.V.; Bonan, G.; Coutinho, D.F.; da Silva, J.M.G. Multiple resonant controllers for uninterruptible power supplies—a systematic robust control design approach. *IEEE Trans. Ind. Electron.* **2014**, *61*, 1528–1538. [[CrossRef](#)]



© 2020 by the author. Licensee MDPI, Basel, Switzerland. This article is an open access article distributed under the terms and conditions of the Creative Commons Attribution (CC BY) license (<http://creativecommons.org/licenses/by/4.0/>).